ADVANCED FUNCTIONAL MATERIALS
www.afm-journal.de

Dual-Site Doping and Low-Angle Grain Boundaries Lead to High Thermoelectric Performance in N-Type Bi_2S_3

Jian Yang, Haolin Ye, Xiangzhao Zhang, Xin Miao, Xiubo Yang, Lin Xie, Zhongqi Shi, Shaoping Chen, Chongjian Zhou, Guanjun Qiao, Matthias Wuttig, Li Wang, Guiwu Liu,* and Yuan Yu**

Bismuth sulfide (Bi_2S_3) is a promising thermoelectric material with earth-abundant, low-cost, and environment-friendly constituents. However, it shows poor thermoelectric performance due to its extremely low electrical conductivity derived from the low electron concentration. Here, a high-performance Bi_2S_3-based material is reported to benefit from the Fermi level tuning by Ag and Cl co-doping and defect engineering by introducing dense low-angle grain boundaries. Both Ag and Cl act as donors in Bi_2S_3, upshifting the Fermi level. This increases the electron concentration without degrading the electron mobility, thereby obtaining improved electrical conductivity. The electron localization function (ELF) contour map indicates that interstitial Ag causes electron delocalization, showing higher electron mobility in Bi_2S_3. More importantly, dense low-angle grain boundaries block phonon propagation, yielding an ultralow lattice thermal conductivity of 0.30 W m^{-1} K^{-1}. Consequently, a record *ZT* value of ≈0.9 at 676 K is achieved in the $Bi_2Ag_{0.01}S_3$-0.5%$BiCl_3$ sample.

1. Introduction

Thermoelectric devices can directly convert heat into electricity without byproduct gas emissions, promising applications in clean energy harvesting.[1] The conversion efficiency of a thermoelectric device is mainly determined by a figure of merit, $ZT = S^2\sigma T/\kappa$, where S, σ, T, and κ are the Seebeck coefficient, electrical conductivity, absolute temperature, and thermal conductivity (involving the electron contribution κ_{ele} and lattice contribution κ_{lat}), respectively.[2] Even though state-of-the-art thermoelectric materials such as lead chalcogenides,[3] Bi_2Te_3,[4] and GeTe[5] exhibit outstanding thermoelectric performance, they contain toxic (Pb), rare (Te), and expensive (Ge) elements.

J. Yang, X. Zhang, G. Qiao, G. Liu
School of Materials Science and Engineering
Jiangsu University
Zhenjiang 212013, China
E-mail: gwliu76@ujs.edu.cn

H. Ye, C. Zhou, L. Wang
State Key Laboratory of Solidification Processing
and Key Laboratory of Radiation Detection Materials and Devices
Ministry of Industry and Information Technology
Northwestern Polytechnical University
Xi'an 710072, China
E-mail: wl0815@skku.edu

X. Miao, S. Chen
School of Materials Science and Engineering
Taiyuan University of Technology
Taiyuan 030024, China

X. Yang
Analytical & Testing Center
Northwestern Polytechnical University
Xi'an 710072, China

L. Xie
Department of Physics
Southern University of Science and Technology
Shenzhen 518055, China

Z. Shi
State Key Laboratory for Mechanical Behavior of Materials
Xi'an Jiaotong University
Xi'an 710049, China

M. Wuttig
PGI 10 (Green IT)
Forschungszentrum Jülich GmbH
52428 Jülich, Germany

M. Wuttig, Y. Yu
Institute of Physics (IA)
RWTH Aachen University
52056 Aachen, Germany
E-mail: yu@physik.rwth-aachen.de

The ORCID identification number(s) for the author(s) of this article can be found under https://doi.org/10.1002/adfm.202306961

DOI: 10.1002/adfm.202306961

Thus, exploring new thermoelectric materials composed of low-toxic, cost-effective, and earth-abundant elements with decent *ZT* values is drawing increasing attention.

In recent years, bismuth sulfide (Bi_2S_3) has been considered an interesting and promising thermoelectric material given its large Seebeck coefficient, low thermal conductivity, as well as environmental-benign and low-cost composition.[6] However, the intrinsically small electrical conductivity of pristine Bi_2S_3 brings about a poor *ZT* value. Differing from its rhombohedral V_2VI_3 counterpart such as Bi_2Te_3, which utilizes metavalent bonding, [7] Bi_2S_3 crystallizes in an orthorhombic structure utilizing covalent bonding.[8] This covalent bonding nature along with a strong Peierls distortion localizes charge carriers leading to a low carrier concentration and small mobility. Indeed, the electron concentration of pristine Bi_2S_3 is on the order of 10^{16}–10^{17} cm^{-3}, which is far lower than the optimum range of 10^{19}–10^{21} cm^{-3} for good thermoelectrics.[1c,5,9] So far, the routine method to tune the electron concentration is realized by chemical doping. It is reported that the substitution of sulfur sites by halogen elements such as through doping with $BiCl_3$,[10] $HfCl_4$,[11] Se-$BiCl_3$,[12] BiI_3,[13] $SbCl_3$,[14] $PbBr_2$,[15] and $CuBr_2$[16] can effectively improve the electron concentration. Besides, the van der Waals (vdW) gap in Bi_2S_3 can largely tolerate the incorporation of interstitial atoms such as Ag and Cu, which also behave as donors.[17] Even though the carrier concentration can be greatly increased by either anion or interstitial dopants, the charge carrier mobility is often decreased at high doping levels due to the increased scattering strength.[15,18] Very interestingly, a simultaneous enhancement of the carrier concentration and mobility has been realized in Cu and Br co-doped layered $SnSe_2$, where Cu and Br occupy the vdW gap and the anion substitutional position, respectively. The strong Cu–Br interaction builds "electrical bridges" to connect $SnSe_2$ interlayers, leading to a record power factor in $SnSe_2$.[19] Given the similar layer structure of Bi_2S_3, a synergistic optimization of the carrier concentration and mobility can also be expected in Bi_2S_3 by the dual-site intercalation and doping strategy.

On the other hand, the increased electrical conductivity will inevitably enhance the thermal transport carried by electrons, which is detrimental to the improvement of *ZT*. This trade-off between charge and heat transport can be counterbalanced by decreasing the lattice's thermal conductivity. Introducing lattice imperfections such as point defects,[20] dislocations,[21] nanopores,[22] and hierarchical architectures[23] can effectively decrease the lattice's thermal conductivity. However, these imperfections can also impede the transport of electrons, reducing the carrier mobility.[24] Additionally, stress engineering is a widely used method to tune the physical properties of a given material, which can modulate the band gap, effective mass, and valley degeneracy at conduction/valance band edges.[25] Meanwhile, tensile strain can soften the phonons, decreasing the phonon group velocity, and thus leading to a reduced thermal conductivity.[26] However, strain-tunable electron/phonon transport is usually achieved in 2D materials with their large stretchability, bendability, and foldability or in 3D bulk samples at high pressure.[27] In contrast, coherent or semi-coherent interfaces are reported to selectively scatter phonons rather than electrons. For example, a significant reduction in the lattice thermal conductivity can be achieved by introducing twin boundaries[28] or low-angle grain boundaries (LAGBs)[29] while maintaining the high charge carrier mobility.[30]

Here, we found that introducing Ag to the van der Waals (vdW) gap and Cl to the substitutional position of sulfur can simultaneously increase the carrier concentration and mobility. This is due to the delocalized electrons provided by intercalated Ag atoms that transfer charge to their neighboring Cl atoms through "electrical bridges". Additionally, a very high density of LAGBs is observed in the doped sample, yielding a low lattice thermal conductivity of 0.30 $W\ m^{-1}\ K^{-1}$. Consequently, a maximum *ZT* value of ≈0.9 at 676 K and an average *ZT* (ZT_{avg}) of ≈0.52 at 323–676 K are achieved, which are both records for Bi_2S_3-based compounds. Our work demonstrates that interstitial and substitutional dual-site doping as well as the introduction of LAGBs in layered compounds can optimize the electrical and thermal transport synergistically.

2. Results and Discussion

2.1. Design Principle

Bi_2S_3 crystallizes in a lamellar structure with an orthorhombic *Pbnm* space group. This material is constructed by interconnecting aligned $(Bi_4S_6)_n$ ribbons connected by strong covalent Bi–S bonds and weak vdW bonds along [100] direction, as schematically illustrated in **Figure 1a**.[17a] These vdW gaps in Bi_2S_3 can be readily intercalated with guest species such as Ag^+ cations, which is conducive to enhancing the charge transport across the gaps. However, intercalants usually are highly mobile and diffuse rapidly along the vdW gap, forming nanoscale precipitates within the matrix.[31] A stronger electron acceptor at the anion site may stabilize the intercalant by Coulomb attraction as well as facilitate the charge transfer.[19,32] Thus, we synthesized several $Bi_2Ag_xS_3$-0.5%$BiCl_3$ ($x = 0$, 0.005, 0.01, and 0.02) samples.

The powder X-ray diffraction (XRD) patterns of $Bi_2Ag_xS_3$-0.5%$BiCl_3$ ($x = 0$, 0.005, 0.01, and 0.02) samples can be fully indexed to Bi_2S_3 without any second phase within the resolution of laboratory XRD (Figure 1b). The lattice parameters along the *c*-axis increase with increasing Ag concentration (Figure 1c), indicating the intercalation of Ag at the vdW gap. The optical absorption spectra resolved the energy gap of pristine Bi_2S_3 to be about 1.27 eV, agreeing with a previous report.[10,17a] In contrast, the title sample $Bi_2Ag_{0.01}S_3$-0.5%$BiCl_3$ exhibits a band gap of ≈1.2 eV (Figure 1d). This indicates that the dual incorporation of Ag and Cl impacts the microstructure and electronic band structure as discussed below.

2.2. Direct Observation of Local Crystal Structure

To directly determine the impact of dual incorporation of Ag and Cl on the microstructure, we investigated the atomic structure of the hot pressing sintering (HP)-processed $Bi_2Ag_{0.01}S_3$-0.5%$BiCl_3$ sample employing a spherical aberration-corrected scanning transmission electron microscope (Cs-STEM). **Figure 2a** presents a low-magnification TEM image, showing the absence of nano-precipitates or dislocations that are commonly found in doped materials. Interestingly, a magnified TEM (HRTEM) image taken

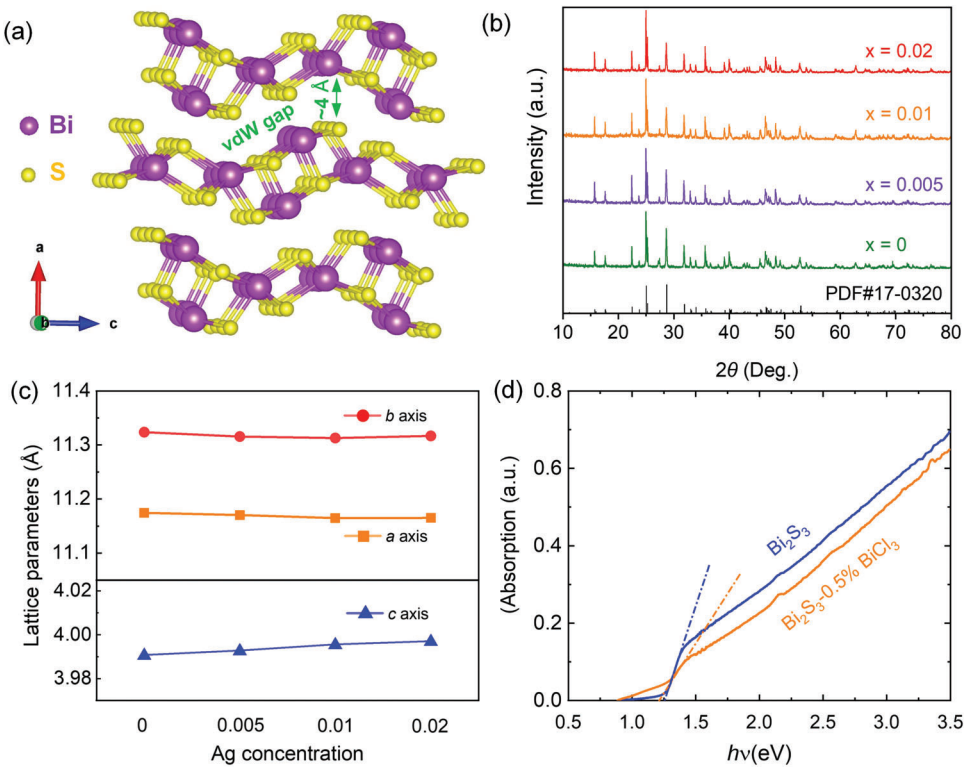

Figure 1. a) The crystal structure of Bi_2S_3; b) Powder X-ray diffraction patterns and c) lattice parameters for the $Bi_2Ag_xS_3$-0.5%$BiCl_3$ samples (x = 0, 0.005, 0.01, and 0.02); d) Optical absorption spectra for Bi_2S_3 and $Bi_2Ag_{0.01}S_3$-0.5%$BiCl_3$ samples as indicated by blue and orange lines, respectively.

from the grain interior reveals a high number density of ultrafine grains with a diameter of ≈5 nm (Figure 2b). We measured the crystallographic misorientation between nanograins in reciprocal space from the corresponding selected area electron diffraction pattern (inset of Figure 2b). The misorientation angles between these grains are smaller than about 10 degrees, indicating the ubiquitous presence of low-angle grain boundaries (LAGBs) within the matrix.

The LAGBs also can be visualized in real space. Figure 2c displays a high-magnification TEM image, which clearly resolves subgrain boundaries. A certain dislocation (marked by "⊥") around the subgrain boundaries can be observed, which is quite easily discernable in the inverse fast Fourier transformation (IFFT) image (inset of Figure 2c). The atomic level microstructures are also collected in the high-angle annular dark field (HAADF) image as exhibited in Figure 2d, which shows different lattice planes of the subgrain and the small misorientation between neighboring grains. These LAGBs form semi-coherent interfaces with strains mediated by dislocation arrays. The corresponding shear strain map profile (ϵ_{xy}) was acquired using geometric phase analysis (GPA). It demonstrates that the strain mainly accumulated at the subgrain boundaries and dissipates rapidly in the surrounding matrix (inset in Figure 2d).

Due to the extremely small grain size, it is challenging to precisely resolve the distribution of constituent elements within the grain and across the grain boundaries by the TEM technique. Alternatively, we analyzed the spatial distribution of the elements in sample $Bi_2Ag_{0.01}S_3$-0.5%$BiCl_3$, employing atom probe tomography (APT) (Figure 2e and Figure S1, Supporting Information).[33] Figure 2e presents the 3D distribution of Ag and Cl atoms denoted by gray and green point clouds, respectively, across a grain boundary. A significant co-segregation of Ag and Cl to the grain boundary can be observed. A close-up of the grain boundary area implies the strong affinity between Ag and Cl atoms. To quantitatively resolve the content of each element with greater statistical accuracy, we extracted 1D compositional profiles across the grain boundary. Figure 2f shows that the composition of the grain interior is close to the nominal Bi_2S_3 with a low content of soluble Ag. In contrast, the concentration of Ag and Cl synchronously increases at the grain boundary. These observations are consistent with our hypothesis that stronger electron acceptor Cl^{-1} could attract Ag^+ cation due to Coulomb interaction facilitating the charge transfer from Ag to the matrix, as we will discuss later.

2.3. Charge Transport Properties

The electrical transport properties for the $Bi_2Ag_xS_3$-0.5%$BiCl_3$ (x = 0, 0.005, 0.01, and 0.02) samples show that Ag and Cl codoping simultaneously increases the carrier concentration (n_H) and carrier mobility (μ_H) (Table S1, Supporting Information). For example, the sample with x = 0.02 exhibits n_H and μ_H of ≈3.68 × 10^{19} cm^{-3} and ≈49.9 cm^2 V^{-1} s^{-1}, respectively. In comparison, those for pristine Bi_2S_3 are ≈1.71 × 10^{17} cm^{-3} and ≈38.3 cm^2 V^{-1} s^{-1}, respectively. We calculated the relationship between μ_H and n_H for pristine Bi_2S_3 at 300 K when acoustic phonon scattering, alloy scattering, and polar optical phonon

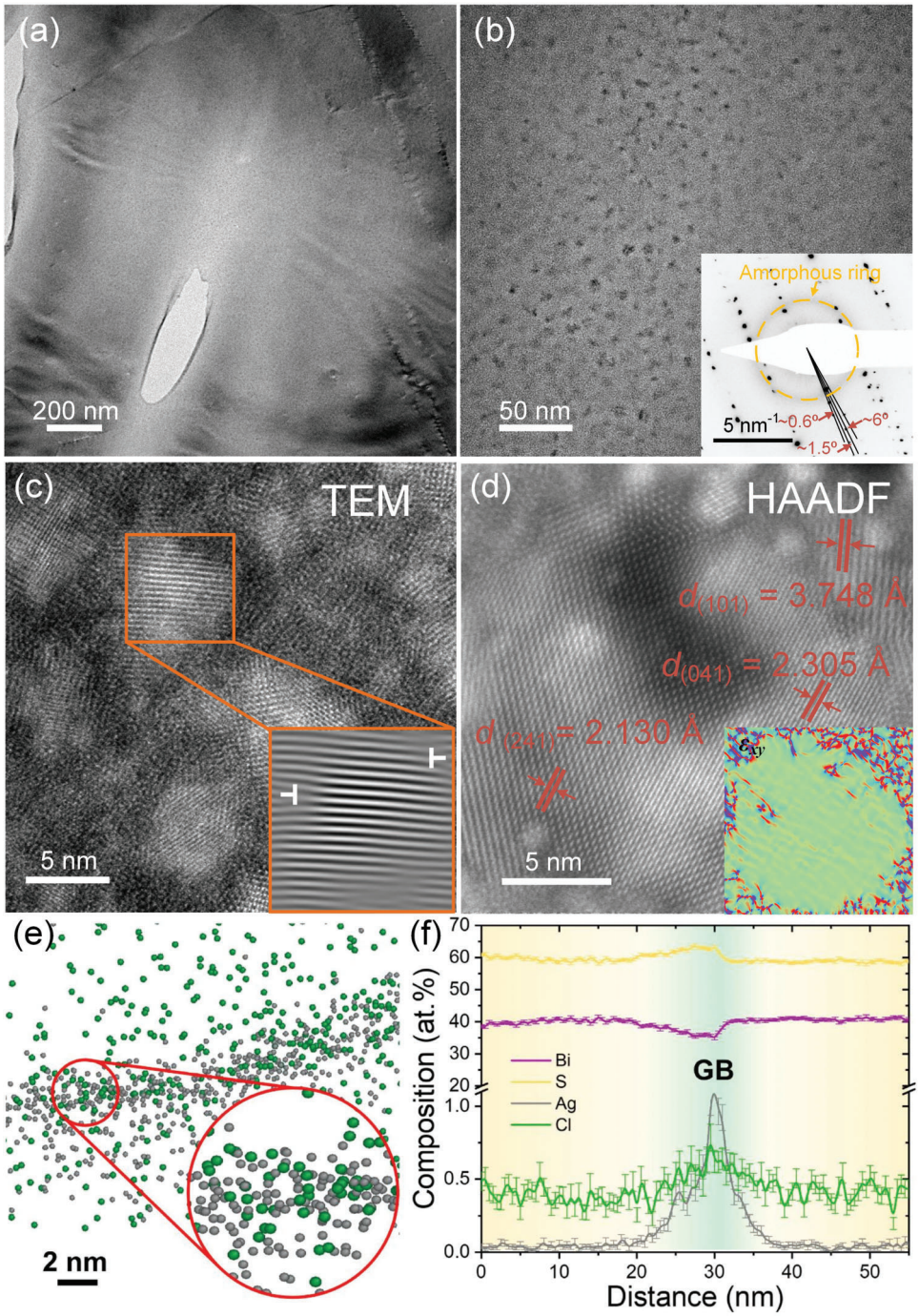

Figure 2. Typical TEM and STEM-HAADF images of $Bi_2Ag_{0.01}S_3$-0.5%$BiCl_3$ sample: a) A TEM image, showing the absence of nanoprecipitates or dislocations; b) TEM images, showing dense subgrains with a size of ≈5 nm. The inset displays the selected area diffraction pattern, showing small misorientation angles between neighboring grains aligned along the same zone axis; c) A magnified TEM image showing dense subgrains within the matrix. Inset: corresponding IFFT image displaying edge dislocations located around the subgrain boundaries as marked by⊥; d) A TEM image, showing the semi-coherent interfaces between subgrains. The inset is the geometric phase analysis (GPA) of the corresponding HAADF image; e) The magnified grain boundary area measured by APT, demonstrating the co-segregation and strong attraction between Cl and Ag atoms. Note that the green points represent the $BiCl^+$ ions rather than single Cl^+ ions as explained in detail in the Supporting Information. f) 1D composition profile across the grain boundary showing the co-aggregation of Ag and Cl at the grain boundary.

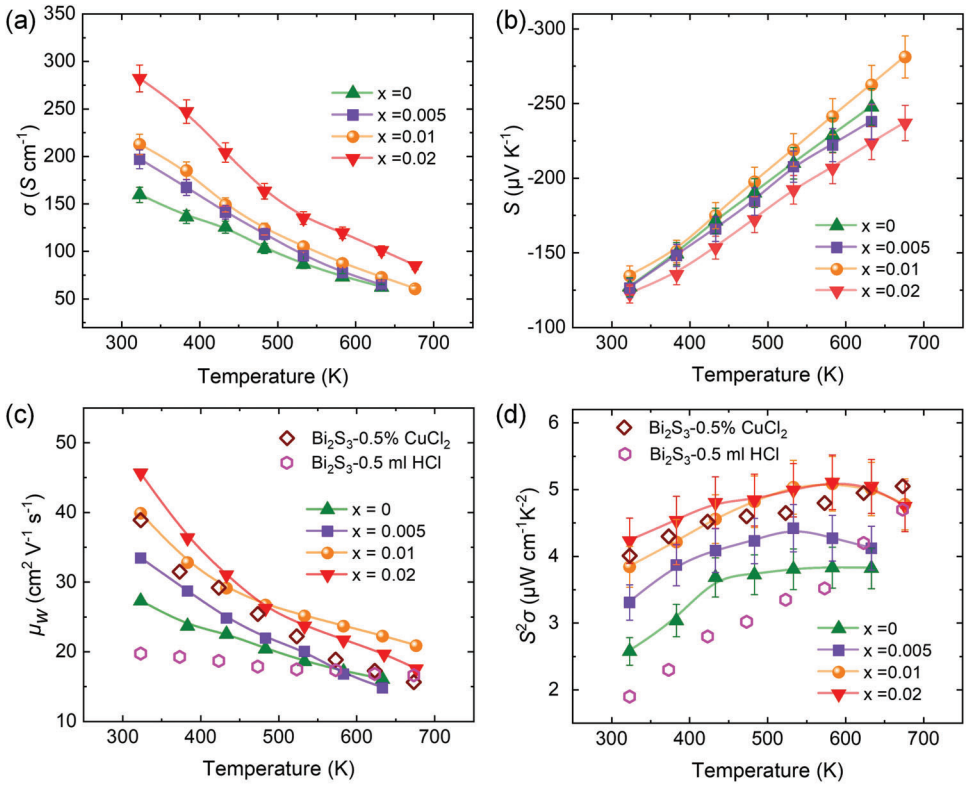

Figure 3. Temperature-dependent a) electrical conductivity, b) Seebeck coefficient, c) weighted mobility, and d) power factor of $Bi_2Ag_xS_3$-0.5% $BiCl_3$ samples. The μ_w and $S^2\sigma$ of Bi_2S_3-0.5 ml HCl[18a] and Bi_2S_3-0.5% $CuCl_2$[18b] are also included for comparison.

scattering are considered the scattering mechanisms for electron transport (Figure S2, Supporting Information). The experimental μ_H at 300 K for doped Bi_2S_3 with various dopants lies far below the theoretical curve. In contrast, the μ_H for the $Bi_2Ag_{0.02}S_3$-0.5%$BiCl_3$ sample falls well on the theoretical line. These observations contradict the general understanding that degenerate semiconductors show decreased μ_H with increasing n_H due to the enhanced carrier-carrier scattering mechanism.[34]

Figure 3a shows the temperature-dependent electrical conductivity (σ) for $Bi_2Ag_xS_3$-0.5%$BiCl_3$ (x = 0, 0.005, 0.01, and 0.02) samples. The σ of all samples monotonously decreases with increasing temperature, consistent with heavily doped semiconductors with apparent metallic transport behavior. The simultaneously increased n_H and μ_H of $Bi_2Ag_xS_3$-0.5%$BiCl_3$ give rise to a significantly improved σ compared with pristine Bi_2S_3 and Bi_2S_3-0.5%$BiCl_3$. For example, the $x = 0.02$ sample shows a σ of 300 S cm^{-1} at room temperature, nearly two times higher than the Ag-free sample. Note that LAGBs described as dislocation arrays have much less effect on the μ_H due to their higher atomic density and lower energy state than that of high-angle grain boundaries.[35] Remarkably, the $Bi_2Ag_{0.02}S_3$-0.5%$BiCl_3$ sample involving ultrafine grains shows a comparable σ to the previously reported 0.5 mol.% $CuCl_2$ doped Bi_2S_3 ingot with micrometer-size grains at the same electron concentration (≈240 S cm^{-1} at 323 K).[18b] This indicates that the very high number density of LAGBs will not strongly deteriorate the σ, as experimentally demonstrated in PbTe.[30b]

The Seebeck coefficient (S) for all the samples is negative over the measured temperature range, indicative of n-type charge transport (Figure 3b). Because pristine Bi_2S_3 has a single conduction band near the Fermi level, the magnitude of S ($|S|$) gradually reduces with the increasing Ag content due to the increased n. We also calculated the theoretical Pisarenko relation between S and n for pristine Bi_2S_3, as shown in Figure S2, Supporting Information. The $Bi_2Ag_xS_3$-0.5%$BiCl_3$ (x = 0.005, 0.01, and 0.02) samples show $|S|$ values far above the Pisarenko line at the given n_H, indicating an enhancement of the density-of-states effective mass by the dual incorporation of Ag and Cl.

To quantify the effect of Ag-Cl interaction on charge transport properties, we calculated the temperature-dependent weighted mobility (μ_w) of $Bi_2Ag_xS_3$-0.5%$BiCl_3$ (x = 0, 0.005, 0.01, and 0.02) samples (See Supporting Information for the calculation details). The data of Bi_2S_3-0.5%CuCl and Bi_2S_3-0.5 ml HCl are also included for comparison. The index μ_w appraises the inherent electronic transport properties of a given thermoelectric material.[36] All Bi_2S_3-based compounds show that μ_w decreases with increasing temperature over the entire temperature investigated, demonstrating a phonon-dominated charge carrier scattering process. Remarkably, the μ_w at 323 K of $Bi_2Ag_xS_3$-0.5%$BiCl_3$ samples monotonously increase from 27.2 cm^2 V^{-1} s^{-1} for Bi_2S_3-0.5%$BiCl_3$ to 45.6 cm^2 V^{-1} s^{-1} for $Bi_2Ag_{0.02}S_3$-0.5%$BiCl_3$ sample. Note that the μ_w of co-doped samples is higher than that of previous Bi_2S_3-0.5%$CuCl_2$ and Bi_2S_3-0.5 ml HCl samples, confirming better inherent electronic transport properties of the Ag-Cl co-doped sample.

The remarkably enhanced σ and relatively high S significantly enhance the power factor (PF) for $Bi_2Ag_xS_3$-0.5%$BiCl_3$ samples (Figure 3d). Specifically, our $Bi_2Ag_{0.01}S_3$-0.5%$BiCl_3$ sample shows PF of 3.84 μW cm^{-1} K^{-2} at 323 K, which gradually rises to 5.01 μW cm^{-1} K^{-2} at 633 K. These values are higher than those of Bi_2S_3-0.5% $CuCl_2$ and Bi_2S_3-0.5 ml HCl samples as indicated by open brown diamonds and open pink hexagonal symbols, respectively. We calculated theoretical $S^2\sigma$ as a function of n_H at 300 K and compared them with the experimental data for our samples and other samples reported in the literature[14,15,18] (Figure S3, Supporting Information). The results show that the PF of our $Bi_2Ag_xS_3$-0.5%$BiCl_3$ samples (x = 0.005, 0.01, and 0.02) match well with the theoretically predicted maximum values. This also indicates that the carrier concentration has been optimized. Typically, it is challenging to realize PF close to the theoretical prediction because optimizing n_H by doping or alloying usually reduces the carrier mobility, which leads to lower experimental PF than the predictions. In contrast, these experimental and theoretical results unambiguously validate that our strategy can enhance $S^2\sigma$ by increasing n_H without deteriorating μ_H.

2.4. Electronic Structures

To better understand the large Seebeck coefficients above the theoretical Pisarenko line in the $Bi_2Ag_xS_3$-0.5%$BiCl_3$ (x = 0, 0.005, 0.01, and 0.02) system, we carried out first-principles density functional theory (DFT) calculations to reveal the electronic band structure. To mimic the experimental configurations, we built the supercells by combining our XRD, STEM, and APT results with previously reported defect calculations.[17a] Specifically, Ag and Cl atoms are placed in the VdW gap along the b-axis and the nearest anion site at the (010) plane of the Bi_2S_3 lattice (Figure S4, Supporting Information), respectively. It is interesting to note that the total energy for $Bi_{24}S_{36}$, $Bi_{24}S_{35}Cl$, and $Bi_{24}AgS_{35}Cl$ are −257.989, −255.852, and −258.441 eV, respectively. This explains the formation mechanism underpinning the ultrafine grains in Figure 2: The dual incorporation of Ag and Cl atoms and their co-segregation to grain boundaries reduce the overall surface energy (−3.934, −3.9616, and −4.004 J m^{-2} for $Bi_{24}S_{36}$, $Bi_{24}S_{35}Cl$, and $Bi_{24}AgS_{35}Cl$, respectively), impeding the grain growth at elevated temperatures.

To evaluate the effect of vdW force correction on the inherent electronic transport properties of the Bi_2S_3-based system, we calculated the electronic band structure of $Bi_{24}S_{35}Cl$ with and without the vdW correction (Figure S5, Supporting Information). The comparisons between the electronic band structures with and without vdW correction indicate that the vdW correction rarely affects the inherent electronic transport properties of the $Bi_2Ag_xS_3$-0.5%$BiCl_3$ system. Therefore, the electronic band structures without the vdW correction can explain accurately the electronic transport properties of $Bi_2Ag_xS_3$-0.5%$BiCl_3$. **Figures** 4a,b shows the electronic band structure of $Bi_{24}S_{35}Cl$ and $Bi_{24}AgS_{35}Cl$, respectively. The solely Cl-doped Bi_2S_3 exhibits a band gap of ≈1.32 eV, consistent with the solid-state optical absorption spectra. The Fermi level E_f of Cl-doped Bi_2S_3 crosses two conduction bands, corresponding to a band degeneracy N_v = 2. In contrast, the dual incorporation of Ag and Cl narrowed the band gap of $Bi_{24}AgS_{35}Cl$ and upshifted the Fermi level into the conduction band.[17a] This leads to conduction band convergence with N_v = 3. A higher band degeneracy implies an enhanced Seebeck at a given n_H, agreeing with the Pisarenko plot predicted by the single parabolic band model.

To better understand the interaction between Ag and Cl atoms and its effect on μ_H and n_H, we calculated the electron localization function (ELF) to directly appraise the interaction of adjacent atoms in the matrix. Figure 4b maps ELF of solely Cl-doped Bi_2S_3 viewed down through the a-axis. The magnitude of ELF at 1 corresponds to a perfect localization of electrons and reduces to 0.5 for full delocalization, which is depicted by a color bar transiting from red to blue color. Note that the substitutional Cl atom shows an ELF value nearly identical to the S atom, suggesting the Cl atom itself does not delocalize the electrons. In striking contrast, in the Ag-Cl co-doped Bi_2S_3, the ELF value around the doped Ag atom is much smaller as indicated by the red arrow, corresponding to an absence of electron pairing. This means that the Ag atom contributes significantly to delocalized electrons. This explains why Ag and Cl co-doped Bi_2S_3 samples show both high n_H and μ_H.

We directly visualized and quantified the charge transfer within the matrix for $Bi_{24}S_{35}Cl$ and $Bi_{24}AgS_{35}Cl$ supercells by performing a charge transfer analysis (Figure 4c,d). In the $Bi_{24}S_{35}Cl$ supercell, charge analysis shows that the Bi atom transfers 0.56 electrons to the Cl atom. For the dual-doped $Bi_{24}AgS_{35}Cl$ supercell, electrons of Ag polarize toward Cl, as indicated by the yellow ellipsoid between Ag and Cl atoms, which implies that these electrons are prone to flow toward Cl. A quantitative Bader charge analysis exhibits that the Ag atom contributes 0.31 electrons to the bonded Cl atom, which further increases the n_H. This observation is consistent with the Hall measurement, which shows that the dual incorporation of Ag and Cl gives rise to an n_H higher than the sole Cl-doped specimen.

2.5. Thermal Transport Properties

Figure 5a presents the temperature-dependent total thermal conductivity (κ_{tot}) for $Bi_2Ag_xS_3$-0.5%$BiCl_3$ samples (x = 0.005, 0.01, and 0.02) and control sample Bi_2S_3-0.5%$BiCl_3$ for comparison. Surprisingly, all the codoped samples show κ_{tot} lower than the control sample over the entire temperature range, whereas the σ rapidly increases with higher Ag concentration. This observation implies that Ag concentration significantly affects phonon transport. Given that κ_{tot} consists of the lattice (κ_{lat}) and electronic thermal (κ_{ele}) conductivities, we isolated the κ_{lat} using Wiedemann–Franz law to reveal the effect of dual incorporation of Ag and Cl on the thermal transport by phonons. All the samples show decreasing κ_{lat} with increasing temperature. Their values continuously decrease with increasing Ag content in the full range of temperatures (Figure 5b). At 323 K, the κ_{lat} decreases from 0.75 W m^{-1} K^{-1} for Cl-doped Bi_2S_3 to 0.55 W m^{-1} K^{-1} for $Bi_2Ag_{0.01}S_3$-0.5%$BiCl_3$. Particularly, $Bi_2Ag_{0.01}S_3$-0.5%$BiCl_3$ has an ultralow κ_{lat} of 0.30 W m^{-1} K^{-1} at 676 K. Figure 5c compared the κ_{lat} of $Bi_2Ag_{0.01}S_3$-0.5%$BiCl_3$ sample with other state-of-the-art Bi_2S_3-based thermoelectrics, demonstrating its lowest κ_{lat} among Bi_2S_3-based compounds. In fact, κ_{lat} of $Bi_2Ag_{0.01}S_3$-0.5%$BiCl_3$ is also lower than any other binary sulfides reported so far. For

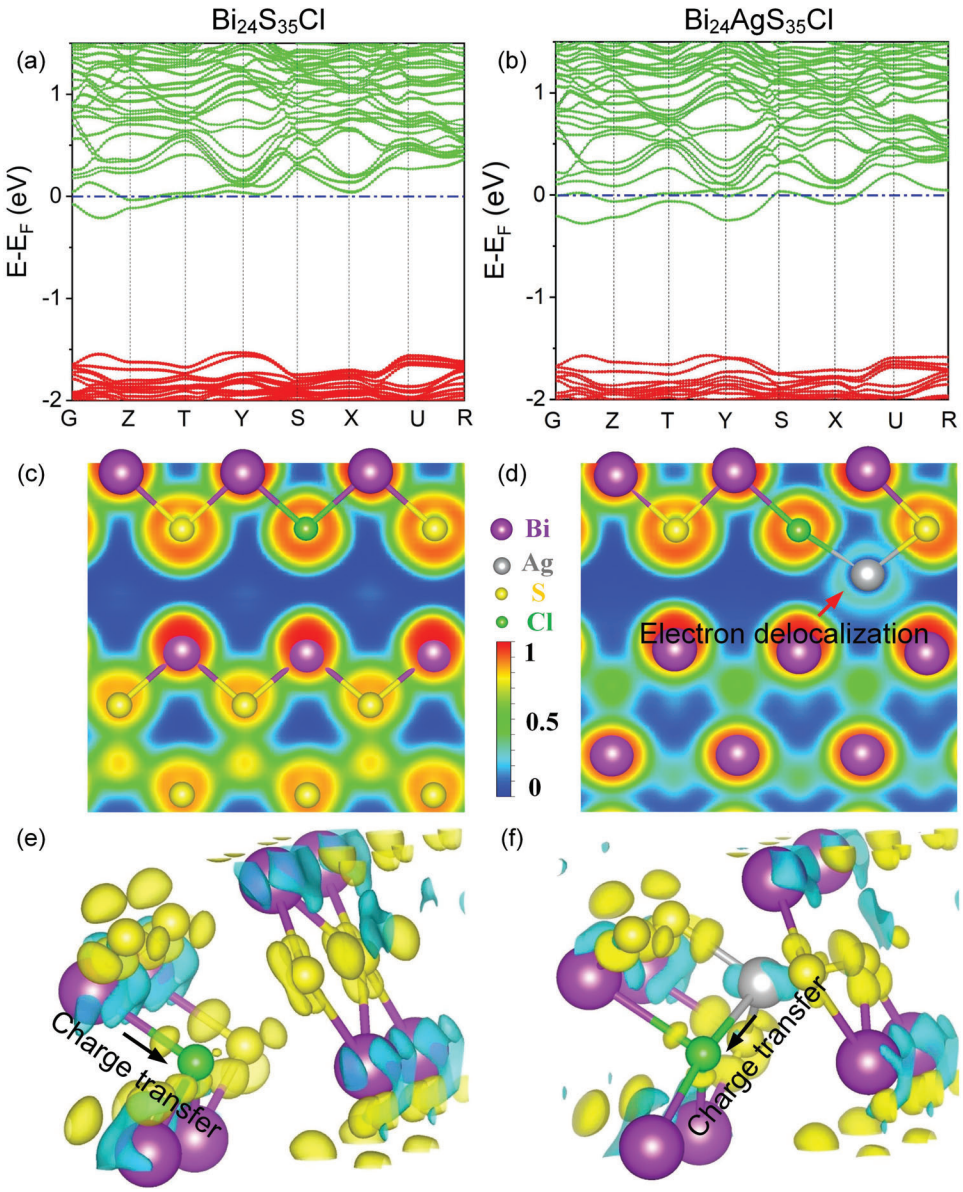

Figure 4. Calculated electronic band structures for a) $Bi_{24}S_{35}Cl$ and b) $Bi_{24}AgS_{25}Cl$ supercells. The Fermi level of doped and pristine Bi_2S_3 is set to 0 eV to visualize the band convergence. (c,d) map the electron localization function (ELF) for $Bi_{24}S_{35}Cl$ and $Bi_{24}AgS_{25}Cl$ along the *a*-axis, respectively. The ELF values ranging from 0 to 1 are shown by the color scheme given in (d). The red arrow in (d) indicates the electron delocalization around the Ag atom. (e,f) present the charge transfer analysis for $Bi_{24}S_{35}Cl$ and $Bi_{24}AgS_{35}Cl$ supercells. Cyan ellipsoids denote a loss of electrons.

example, the κ_{lat} at 676 K for PbS,[37] SnS,[38] and Cu_2S[39] are 0.9, 0.8, and 0.6 W m^{-1} K^{-1}, respectively.

To better understand the exceptionally low κ_{lat} in Bi_2S_3, we calculated the phonon dispersion interactions and group velocities based on the three-phonon scattering processes (Figure S7, Supporting Information). It is clear that the optical phonons above 15 meV are heavily damped by three-phonon interactions. The spectral functions for the phonons with energies below 15 meV are comparatively sharper, indicating weaker three-phonon interactions. Meanwhile, the flat low-frequency optical phonon bunching indicates the low group velocity of phonons. Noticeably, the acoustic modes are fairly soft with a maximum value of ≈3.5 km s^{-1} at the zone-center Gamma point, and the group velocities of a large number of phonons in Bi_2S_3 are significantly smaller than ≈2 km s^{-1} and even below 1 km s^{-1}. Such dramatically low group velocities lead to low lattice thermal conductivity, which may be attributed to the weak bonding strength between the laminated structure of Bi_2S_3.[15] Nevertheless, we note that the flat optical phonon bunching at ≈5 meV could lead to large four-phonon scattering phase space and thus give rise to strong four-phonon scatterings. Indeed, for some bulk materials with unique phonon dispersion curves such as a large-frequency band gap,[40] the flatness of phonon branches,[41] and acoustic bunching,[42] the lowest order three-phonon scattering process fails to accurately predict the lattice thermal conductivity. The higher-order anharmonicity plays a non-negligible role in the

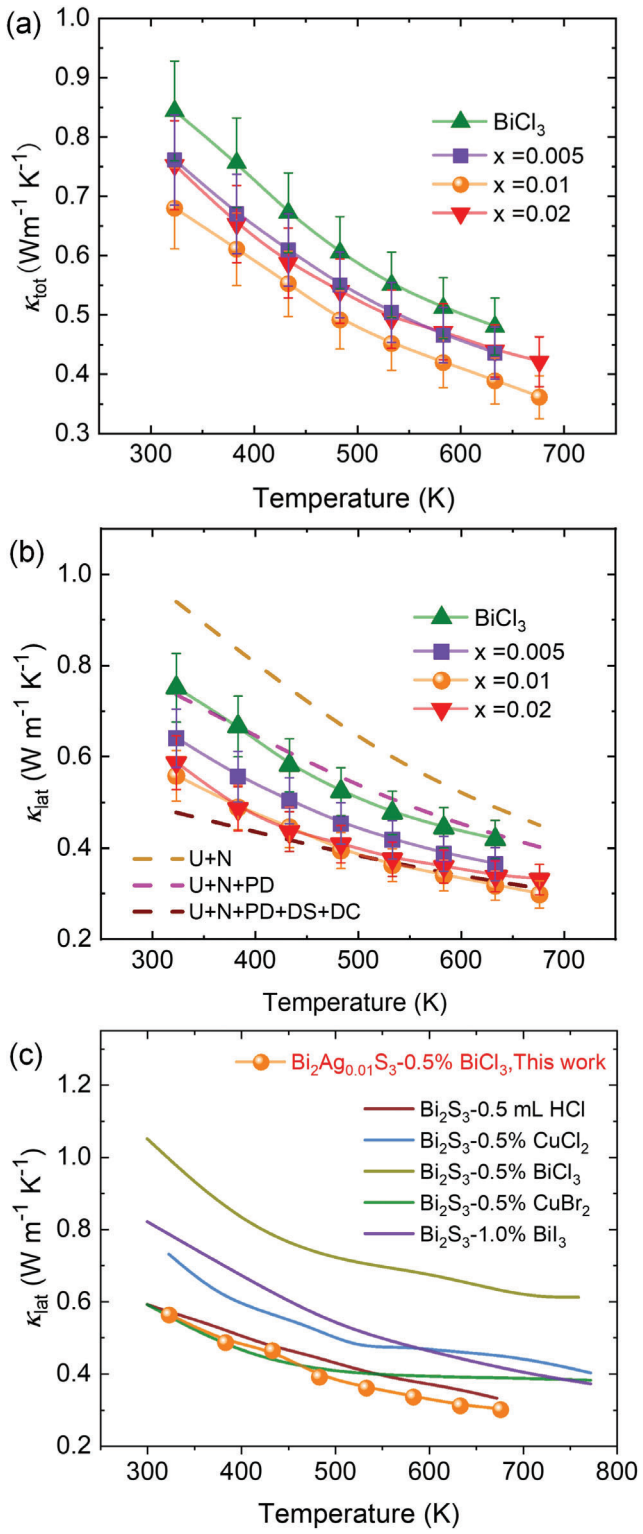

Figure 5. Temperature dependence of thermal transport properties of $Bi_2Ag_xS_3$-0.5%$BiCl_3$ samples: a) Thermal conductivity, b) lattice thermal conductivity and Debye–Callaway modeling results; c) A comparison of lattice thermal conductivity of as-fabricated $Bi_2Ag_{0.01}S_3$-0.5%$BiCl_3$ and other superior Bi_2S_3-based materials.[10,13,16,18a,b]

thermal transport of these bulk materials.[43] Unfortunately, our calculation source is not enough to calculate the four-phonon interactions even with a very coarse *k*-mesh grid 3 × 4 × 3 due to the complexity of the Bi_2S_3 system, which has a total number of 20 atoms in a primitive cell. Nevertheless, Bi_2S_3 could be an interesting system for studying the four-phonon interactions. With the doping and intercalation to introduce complex structural defects, the lattice thermal conductivity is further decreased. Thus, we calculated the temperature-dependent κ_{lat} of $Bi_2Ag_{0.01}S_3$-0.5%$BiCl_3$ by recalling the modified Debye–Callaway model (dash lines in Figure 5b, See Supporting Information for details). We considered various scattering events present in the samples from our STEM observations including the normal (N) and Umklapp (U) processes, point defects (PD), and low-angle grain boundaries (LAGBs). Note that the dense LAGBs are replaced by dislocations in modeling because they are equivalent in phonon scattering.[30b,44] The pink and blue lines represent the calculated κ_{lat} for $Bi_2Ag_{0.01}S_3$-0.5%$BiCl_3$ considering point defects only, and with dislocations, respectively. The calculated κ_{lat} of the latter matches well with the experimental data nearly in the full temperature window, indicating that the observed low κ_{lat} can be attributed to the presence of dense subgrains.

2.6. ZT Values and Efficiency

Figure 6 shows the temperature-dependent *ZT* of $Bi_2Ag_xS_3$-0.5%$BiCl_3$ ($x = 0$, 0.005, 0.01, and 0.02) samples. Other reported high-performance Bi_2S_3-based materials are included for comparison. The simultaneous enhancement in $S^2\sigma$ and reduction in κ result in the exceptionally high *ZT* values at 323–676 K for the $Bi_2Ag_{0.01}S_3$-0.5%$BiCl_3$ sample. Consequently, a record-high *ZT* of ≈0.9 at 676 K is achieved. This *ZT* value is higher than or comparable to the reported ones of the Bi_2S_3 system over the whole temperature range measured (Figure 6b and Table S2, Supporting Information). More importantly, the average *ZT* (ZT_{avg}) value, which evaluates the thermoelectric efficiency more accurately, reaches ≈0.52 at 323–676 K, which is the highest in those of Bi_2S_3-based materials (Figure S8, Supporting Information).

Given the sample is stable without any evaporation at elevated temperatures (Figure S9, Supporting Information), we measured its conversion efficiency in single-leg form. The Sn-Pb alloy was used as a solder layer to bond the Cu electrode and the $Bi_2Ag_{0.01}S_3$-0.5 mol%$BiCl_3$ sample with a dimension of 3 × 3 × 7 mm^3 as depicted in **Figure 7a**. The temperature difference (ΔT) was set as 25, 75, 175, and 275 K, along with cold-side temperature remained a constant at 300 K. Figures 7b, 7c, and 7d present the measured output voltage (*V*), output power (P_{out}), and conversion efficiency (η) as a function of current, respectively. At the ΔT = 275 K and *I* = 0.34 A, we obtained a peak η, P_{out} of ≈0.4% and 6 mW, respectively. The low efficiency is possibly due to several factors. First, the measurement system has a heating plate (≈250 mm in diameter) that is several times larger than the single leg, leading to significant heat loss. Second, Sulfur is highly reactive with common metallic contacts, such as Pb-Sn alloy in this case. Third, an appropriate interfacial thermoelectric material with low contact resistance has not yet been identified for Bi_2S_3.[46] Assembling multi-leg devices with proper *p*-type leg and inert diffusion materials would greatly improve efficiency.[18a,47]

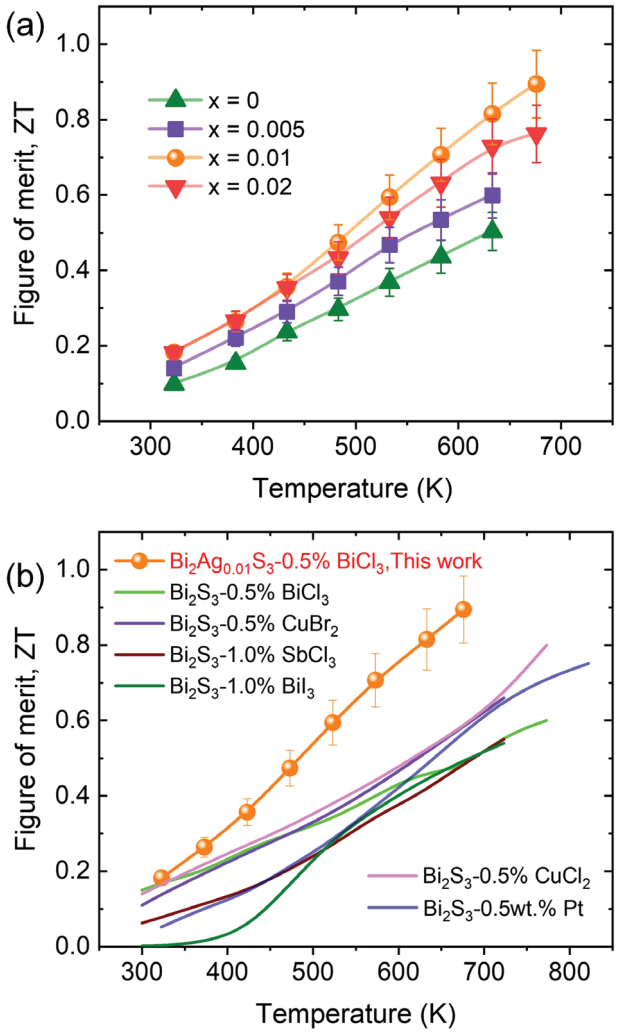

Figure 6. a) Temperature-dependent ZT of $Bi_2Ag_xS_3$-0.5 mol%$BiCl_3$ samples; b) A comparison of ZT between the optimal $Bi_2Ag_{0.01}S_3$-0.5%$BiCl_3$ sample and other related Bi_2S_3-based materials.[10,13,14,16,18b,45]

3. Conclusion

Dual incorporation of Ag and Cl is introduced to improve the thermoelectric performance of earth-abundant Bi_2S_3-based compounds. Both experiments and DFT calculations reveal that Ag and Cl will attract each other forming nearest pairs. Intercalating Ag into the vdW gap of Bi_2S_3 can provide delocalized electrons. These electrons can be more effectively transferred to the matrix through the "electric bridge" between Ag-Cl pairs, which increases the charge carrier concentration without degrading the carrier mobility of the system. The increased carrier concentration moves the Fermi level into the conduction band, crossing more band valleys and increasing the total band degeneracy. Thus, a high Seebeck coefficient can be maintained upon the increased carrier concentration. A high $S^2\sigma$ of 5.01 μW cm^{-1} K^{-2} is achieved at 633 K. The κ of $Bi_2Ag_xS_3$-y%$BiCl_3$ samples is also decreased compared with pristine Bi_2S_3 although the κ_{ele} is enhanced. Dense low-angle grain boundaries are produced in the Ag and Cl dual-doped Bi_2S_3-based materials, which play a critical role in suppressing the propagation of phonons, resulting in an ultralow κ_{lat} of ≈0.30 W m^{-1} K^{-1}. Remarkably, a ZT value of ≈0.9 at 676 K and an average ZT_{avg} value of ≈0.52 at 323–676 K are achieved in the $Bi_2Ag_{0.01}S_3$-0.5%$BiCl_3$ sample, both are records reported so far for Bi_2S_3-based compounds.

4. Experimental Section

Synthesis and Sintering: Ingots with nominal compositions of $Bi_2Ag_xS_3$-y mol.% $BiCl_3$ (abbreviated as $Bi_2Ag_xS_3$-y % $BiCl_3$, x = 0, 0.005, 0.01, and 0.02) were prepared using high-purity Ag (99.99%), Bi (99.999%), S (99.99%), and $BiCl_3$ (99.99%) as starting materials. The mixture of raw materials was put into quartz tubes and sealed at a pressure of 10^{-3} Pa. The tubes were slowly heated to 673 K at a rate of 35 K h^{-1}, soaked for 6 h, and then to 1223 K in 8 h, held at 1223 K for 12 h, and subsequently cooled to 773 K in 8 h, held at 773 K for 48 h. Finally, the as-obtained ingots were cooled down to room temperature for over 20 h. The as-fabricated ingots were hand-ground to powders in an agate mortar. After that, the powders were loaded into graphite dies of Ø12.7 mm and then sintered by hot pressing (HP) process at 723 K for 30 min under an axial pressure of 50 MPa in an Ar atmosphere.

X-ray Powder Diffraction: The powders were examined using X-ray diffraction (XRD, D/MAX-2500 PC) with Cu Kα (λ = 1.5406 Å) radiation.

Transmission Electron Microscopy: For cross-sectional scanning TEM (STEM), specimens were thinned down by focused ion beams (FIB, Helios 650, FEG, FEI) with a dual beam microscope employing gallium ion milling. Structures were analyzed by a spherical aberration-corrected JEM ARM-200F microscope (Cold FEG Type, JEOL). In high-angle annular dark-field (HAADF) STEM images, the point-to-point resolution was about 80 pm after the spherical aberration correction and the angular range of the annular detector employed was from 68 to 280 mrad. All STEM images were obtained by a high-resolution CCD detector with a 2k × 2k pixel device in the GIF-QuantumER imaging filter (GATAN).

Atom Probe Tomography: Needle-shaped APT specimens were prepared by the site-specific "lift-out" method, using a dual-beam scanning electron microscope/focused ion beam (Helios NanoLab 650, FEI). The specimens were measured in a local electrode atom probe (LEAP 5000 XS, Cameca) by applying 10 ps, 3 pJ UV (wavelength = 355 nm) laser pulses with a pulse repetition rate of 200 kHz. The detection rate was two ions per 100 pulses on average (2%) and the ion flight path was 100 mm. The base temperature of the specimen was set at 30 K to minimize the atom diffusions. The detection efficiency of this microscope was limited to 80% owing to the open area left between the microchannels on the detector plates. The APT data were processed using the commercial software package AP Suite 6.1.

DSC and Band Gap Measurement: The heat flow and thermal gravimetric analysis (TGA) were measured by differential scanning calorimetry (DSC) using a Netzsch 449F3 apparatus. The absorption coefficient measurements and UV absorption spectra analyses were performed on the powders using Perkin–Elmer Lambda 950 UV–vis–NIR spectrophotometer.

Thermoelectric Properties Measurement: The electrical conductivity (σ) and Seebeck coefficient (S) were simultaneously measured under a helium atmosphere on an LSR-3 instrument (LINSEIS, LSR-3, Germany) at 323–676 K. The samples for measurement are the square bars with dimensions of 10 × 2 × 2 mm. The thermal diffusivity, D, was measured using the flash diffusivity method in an LFA-457 system (Netzsch, Germany) under an argon atmosphere (Figure S9, Supporting Information). The heat capacity was obtained using Dulong–Petit's law. The thin disks with 10 mm in diameter and 2 mm in thickness were used for the measurements. The thermal conductivity, κ, was calculated using the formula, $\kappa = DC_p\rho$, where ρ is the density of bulk samples, specified using the Archimedes method (Table S1, Supporting Information). All the data were collected along the direction perpendicular to the press direction unless noted otherwise. The uncertainties of S, σ, and κ measurements were about 5%, 5%, and 10%, respectively. The room-temperature Hall coefficient, R, was measured by the four-probe van der Pauw method. The conversion efficiency (η) of

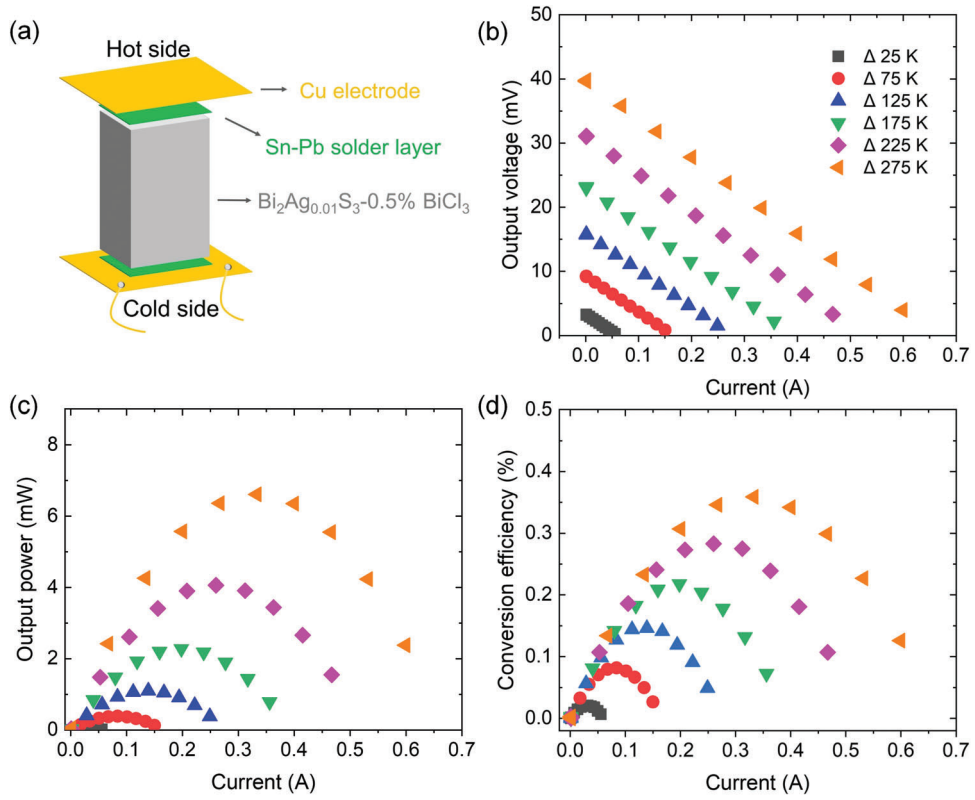

Figure 7. a) Schematic diagram depicts the single leg used for measuring conversion efficiency; The experimentally measured b) output voltage, c) output power, and d) conversion efficiency with respect to electric current of the $Bi_2Ag_{0.01}S_3$-0.5%$BiCl_3$ sample.

the single-leg module was measured by a mini-PEM instrument (Advance Riko) under vacuum, using a nominal hot-side temperature at 300–573 K in a sampling interval of 25 K. The hot and cold sides of the single-leg were welded by tin-based solder, and copper wires were soldered on the copper substrates. The output power (P_{out}) under varied loads was determined by $P_{out} = VI$, (V is the measured terminal voltage and I is the electrical current).

DFT Calculations: The first-principles calculations were performed using the Vienna ab initio simulation package (VASP) code.[48] The exchange-correlation function was described by the generalized gradient approximation (GGA) within the Perdew–Burke–Ernzerhof (PBE).[49] A plane-wave cutoff energy of 500 eV was adopted. A 3 × 1 × 1 supercell containing 60 atoms was used to model the doped structure. A convergence threshold of 0.01 eV $Å^{-1}$ in force was required to reach for all the atoms. The Γ-centered k-point meshes with a k-spacing of ≈0.2 $Å^{-1}$ were employed for structural relaxation and electronic calculations. The PBE without the spin-orbit coupling (SOC) was performed for band structure and density of states (DOS) calculations.

Supporting Information

Supporting Information is available from the Wiley Online Library or from the author.

Acknowledgements

J.Y., H.Y., and X.Z. contributed equally to this work. This work was supported by the National Natural Science Foundation of China (52172069, 51572111), the Natural Science Foundation (BK20210779), the Universities Natural Science Research Project (21KJB430019), the Qing Lan Project ([2016]15) and the Innovation/Entrepreneurship Program ([2021]) of Jiangsu Province. M.W. and Y.Y. acknowledge support from the German Research Foundation DFG within project SFB917. C.Z. acknowledges the financial support from Fundamental Research Funds for the Central University (D5000220051). The authors are thankful for the High-Performance Computing Platform of Jiangsu University.

Open access funding enabled and organized by Projekt DEAL.

Conflict of Interest

The authors declare no conflict of interest.

Data Availability Statement

The data that support the findings of this study are available from the corresponding author upon reasonable request.

Keywords

bismuth sulfide, dual-site doping, electron delocalization, low-angle grain boundary, thermoelectric

Received: June 19, 2023
Revised: November 10, 2023
Published online: December 4, 2023

[1] a) G. J. Snyder, E. S. Toberer, *Nat. Mater.* **2012**, *11*, 422; b) K. F. Hsu, S. Loo, F. Guo, W. Chen, J. S. Dyck, C. Uher, T. Hogan, E. K. Polychroniadis, M. G. Kanatzidis, *Science* **2004**, *303*, 818; c) C. J. Zhou, Y. K. Lee, Y. Yu, S. Byun, Z. Z. Luo, H. Lee, B. Z. Ge, Y. L. Lee, X.

Q. Chen, J. Y. Lee, O. Cojocaru-Mirédin, H. Chang, J. Im, S. P. Cho, M. Wuttig, V. P. Dravid, M. G. Kanatzidis, I. Chung, *Nat. Mater.* **2021**, *20*, 1378; d) J. D. Musah, A. M. Ilyas, S. Venkatesh, S. Mensah, S. Kwofie, V. A. L. Roy, C. M. L. Wu, *Nano Res. Energy* **2022**, *1*, 9120034.

[2] a) J. Yang, G. Liu, Z. Shi, J. Lin, X. Ma, Z. Xu, G. Qiao, *Mater. Today Energy* **2017**, *3*, 72; b) X. Shi, X. Ai, Q. Zhang, X. Lu, S. Gu, L. Su, L. Wang, W. Jiang, W. Jiang, *J. Adv. Ceram.* **2020**, *9*, 424.

[3] a) K. Biswas, J. He, Q. Zhang, G. Wang, C. Uher, V. P. Dravid, M. G. Kanatzidis, *Nat. Chem.* **2011**, *3*, 160; b) C. Zhou, Y. Yu, Y. K. Lee, O. Cojocaru-Mirédin, B. Yoo, S.-P. Cho, J. Im, M. Wuttig, T. Hyeon, I. Chung, *J. Am. Chem. Soc.* **2018**, *140*, 15535.

[4] Y. L. Chen, J. G. Analytis, J.-H. Chu, Z. K. Liu, S.-K. Mo, X. L. Qi, H. J. Zhang, D. H. Lu, X. Dai, Z. Fang, S. C. Zhang, I. R. Fisher, Z. Hussain, Z.-X. Shen, *Science* **2009**, *325*, 178.

[5] M. Hong, K. Zheng, W. Lyv, M. Li, X. Qu, Q. Sun, S. Xu, J. Zou, Z.-G. Chen, *Energy Environ. Sci.* **2020**, *13*, 1856.

[6] J. Pei, L. J. Zhang, B. P. Zhang, P. P. Shang, Y. C. Liu, *J. Mater. Chem. C* **2017**, *5*, 12492.

[7] M. Wuttig, V. L. Deringer, X. Gonze, C. Bichara, J. Y. Raty, *Adv Mater* **2018**, *30*, 1803777.

[8] a) Y. Cheng, O. Cojocaru-Mirédin, J. Keutgen, Y. Yu, M. Küpers, M. Schumacher, P. Golub, J.-Y. Raty, R. Dronskowski, M. Wuttig, *Adv. Mater.* **2019**, *31*, 1904316; b) Y. Yu, M. Cagnoni, O. Cojocaru-Mirédin, M. Wuttig, *Adv. Funct. Mater.* **2020**, *30*, 1904862.

[9] a) Y. Yu, C. Zhou, X. Zhang, L. Abdellaoui, C. Doberstein, B. Berkels, B. Ge, G. Qiao, C. Scheu, M. Wuttig, O. Cojocaru-Mirédin, S. Zhang, *Nano Energy* **2022**, *101*, 107576; b) J. Yang, X. Zhang, G. Liu, L. Zhao, J. Liu, Z. Shi, J. Ding, G. Qiao, *Nano Energy* **2020**, *74*, 104826.

[10] K. Biswas, L.-D. Zhao, M. G. Kanatzidis, *Adv. Energy Mater.* **2012**, *2*, 634.

[11] R. Chmielowski, D. Péré, C. Bera, I. Opahle, W. Xie, S. Jacob, F. Capet, P. Roussel, A. Weidenkaff, G. K. H. Madsen, G. Dennler, *J. Appl. Phys.* **2015**, *117*, 125103.

[12] Y. Chen, D. Y. Wang, Y. L. Zhou, Q. T. Pang, J. W. Shao, G. T. Wang, J. F. Wang, L. D. Zhao, *Front. Phys.* **2019**, *14*, 013601.

[13] J. Yang, G. Liu, J. Yan, X. Zhang, Z. Shi, G. Qiao, *J. Alloys Compd.* **2017**, *728*, 351.

[14] J. Yang, J. Yan, G. Liu, Z. Shi, G. Qiao, *J. Eur. Ceram. Soc.* **2019**, *39*, 1214.

[15] J. Guo, Y.-X. Zhang, Z.-Y. Wang, F. Zheng, Z.-H. Ge, J. Fu, J. Feng, *Nano Energy* **2020**, *78*, 105227.

[16] Z. Liu, Y. Pei, H. Geng, J. Zhou, X. Meng, W. Cai, W. Liu, J. Sui, *Nano Energy* **2015**, *13*, 554.

[17] a) D. Han, M. H. Du, C. M. Dai, D. Y. Sun, S. Y. Chen, *J. Mater. Chem. A* **2017**, *5*, 6200; b) J. Yang, L. Yu, T. Wang, J. Yan, G. Liu, Z. Shi, G. Qiao, *J. Alloys Compd.* **2019**, *780*, 35.

[18] a) J. Guo, J. Yang, Z.-H. Ge, B. Jiang, Y. Qiu, Y.-K. Zhu, X. Wang, J. Rong, X. Yu, J. Feng, J. He, *Adv. Funct. Mater.* **2021**, *31*, 2102838; b) W. Ji, X.-L. Shi, W.-D. Liu, H. Yuan, K. Zheng, B. Wan, W. Shen, Z. Zhang, C. Fang, Q. Wang, L. Chen, Y. Zhang, X. Jia, Z.-G. Chen, *Nano Energy* **2021**, *87*, 106171; c) Y. Wu, Q. Lou, Y. Qiu, J. Guo, Z.-Y. Mei, X. Xu, J. Feng, J. He, Z.-H. Ge, *Inorg. Chem. Front.* **2019**, *6*, 1374.

[19] C. Zhou, Y. Yu, X. Zhang, Y. Cheng, J. Xu, Y. K. Lee, B. Yoo, O. Cojocaru-Mirédin, G. Liu, S.-P. Cho, M. Wuttig, T. Hyeon, I. Chung, *Adv. Funct. Mater.* **2020**, *30*, 1908405.

[20] X. Guo, Z. Chen, J. Tang, F. Zhang, Y. Zhong, H. Liu, R. Ang, *Appl. Phys. Lett.* **2020**, *116*, 103901.

[21] C. Zhou, Y. K. Lee, J. Cha, B. Yoo, S.-P. Cho, T. Hyeon, I. Chung, *J. Am. Chem. Soc.* **2018**, *140*, 9282.

[22] X. Shi, A. Wu, W. Liu, R. Moshwan, Y. Wang, Z.-G. Chen, J. Zou, *ACS Nano* **2018**, *12*, 11417.

[23] a) Y. Zheng, Q. Zhang, X. Su, H. Xie, S. Shu, T. Chen, G. Tan, Y. Yan, X. Tang, C. Uher, G. J. Snyder, *Adv. Energy Mater.* **2015**, *5*, 1401391; b) K. Biswas, J. He, I. D. Blum, C.-I. Wu, T. P. Hogan, D. N. Seidman, V. P. Dravid, M. G. Kanatzidis, *Nature* **2012**, *489*, 414; c) Y. Pei, G. Tan, D. Feng, L. Zheng, Q. Tan, X. Xie, S. Gong, Y. Chen, J.-F. Li, J. He, M. G. Kanatzidis, L.-D. Zhao, *Adv. Energy Mater.* **2017**, *7*, 1601450.

[24] a) A. D. Lalonde, Y. Pei, H. Wang, G. Jeffrey Snyder, *Mater. Today* **2011**, *14*, 526; b) Z. Chen, B. Ge, W. Li, S. Lin, J. Shen, Y. Chang, R. Hanus, G. J. Snyder, Y. Pei, *Nat. Commun.* **2017**, *8*, 13828.

[25] a) D. I. Bilc, D. Benea, V. Pop, P. Ghosez, M. J. Verstraete, *J. Phys. Chem. C* **2021**, *125*, 27084; b) W. Zhou, H. Gong, X. Jin, Y. Chen, H. Li, S. Liu, *Front. Phys.* **2022**, *10*, 842789.

[26] N. Wei, L. Xu, H.-Q. Wang, J.-C. Zheng, *Nanotechnology* **2011**, *22*, 105705.

[27] L.-C. Chen, P.-Q. Chen, W.-J. Li, Q. Zhang, V. V. Struzhkin, A. F. Goncharov, Z. Ren, X.-J. Chen, *Nat. Mater.* **2019**, *18*, 1321.

[28] a) Y. Yu, D.-S. He, S. Zhang, O. Cojocaru-Mirédin, T. Schwarz, A. Stoffers, X.-Y. Wang, S. Zheng, B. Zhu, C. Scheu, D. Wu, J.-Q. He, M. Wuttig, Z.-Y. Huang, F.-Q. Zu, *Nano Energy* **2017**, *37*, 203; b) B. B. Lu, M. Y. Wang, J. Yang, H. G. Hou, X. Z. Zhang, Z. Q. Shi, J. L. Liu, G. J. Qiao, G. W. Liu, *Appl. Phys. Lett.* **2022**, *120*, 173901.

[29] S. I. Kim, K. H. Lee, H. A. Mun, H. S. Kim, S. W. Hwang, J. W. Roh, D. J. Yang, W. H. Shin, X. S. Li, Y. H. Lee, G. J. Snyder, S. W. Kim, *Science* **2015**, *348*, 109.

[30] a) Y. Yu, M. Wuttig, *Nano Res. Energy* **2023**, *2*, 9120057; b) R. Wu, Y. Yu, S. Jia, C. J. Zhou, O. Cojocaru-Mirédin, M. Wuttig, *Nat. Commun.* **2023**, *14*, 719.

[31] a) M.-K. Han, K. Ahn, H. Kim, J.-S. Rhyee, S.-J. Kim, *J. Mater. Chem.* **2011**, *21*, 11365; b) Y. Luo, J. Yang, G. Li, M. Liu, Y. Xiao, L. Fu, W. Li, P. Zhu, J. Peng, S. Gao, J. Zhang, *Adv. Energy Mater.* **2014**, *4*, 1300599.

[32] C. Liu, Z. Huang, D. Wang, X. Wang, L. Miao, X. Wang, S. Wu, N. Toyama, T. Asaka, J. Chen, E. Nishibori, L.-D. Zhao, *J. Mater. Chem. A* **2019**, *7*, 9761.

[33] Y. Yu, C. Zhou, S. Zhang, M. Zhu, M. Wuttig, C. Scheu, D. Raabe, G. J. Snyder, B. Gault, O. Cojocaru-Mirédin, *Mater. Today* **2020**, *32*, 260.

[34] J. Dong, Y. Jiang, J. Liu, J. Pei, X. Y. Tan, H. Hu, A. Suwardi, N. Jia, C. Liu, Q. Zhu, Q. Yan, J.-F. Li, *Nano Energy* **2022**, *103*, 107809.

[35] a) C. Wang, K. Du, K. Song, X. Ye, L. Qi, S. He, D. Tang, N. Lu, H. Jin, F. Li, H. Ye, *Phys. Rev. Lett.* **2018**, *120*, 186102; b) D. Dimos, P. Chaudhari, J. Mannhart, F. K. Legoues, *Phys. Rev. Lett.* **1988**, *61*, 219; c) X. Meng, Z. Liu, B. Cui, D. Qin, H. Geng, W. Cai, L. Fu, J. He, Z. Ren, J. Sui, *Adv. Energy Mater.* **2017**, *7*, 1602582.

[36] G. J. Snyder, A. H. Snyder, M. Wood, R. Gurunathan, B. H. Snyder, C. N. Niu, *Adv. Mater.* **2020**, *32*, 2001537.

[37] Z.-Z. Luo, S. Cai, S. Hao, T. P. Bailey, H. Xie, T. J. Slade, Y. Liu, Y. Luo, Z. Chen, J. Xu, W. Luo, Y. Yu, C. Uher, C. Wolverton, V. P. Dravid, Z. Zou, Q. Yan, M. G. Kanatzidis, *J. Am. Chem. Soc.* **2022**, *144*, 7402.

[38] W. He, D. Wang, H. Wu, Y. Xiao, Y. Zhang, D. He, Y. Feng, Y.-J. Hao, J.-F. Dong, R. Chetty, L. Hao, D. Chen, J. Qin, Q. Yang, X. Li, J.-M. Song, Y. Zhu, W. Xu, C. Niu, X. Li, G. Wang, C. Liu, M. Ohta, S. J. Pennycook, J. He, J.-F. Li, L.-D. Zhao, *Science* **2019**, *365*, 1418.

[39] Y. Yu, D. Yang, J. Li, M. Zhang, H. Luo, Q. Liang, H. Ye, Q. Zhang, X. Tang, J. Wu, *Adv. Funct. Mater.* **2022**, *32*, 2107284.

[40] N. K. Ravichandran, D. Broido, *Phys. Rev. X* **2020**, *10*, 021063.

[41] L. Xie, J. H. Feng, R. Li, J. Q. He, *Phys. Rev. Lett.* **2020**, *125*, 245901.

[42] X. Yang, T. Feng, J. Li, X. Ruan, *Phys. Rev. B* **2019**, *100*, 245203.

[43] a) T. Feng, L. Lindsay, X. Ruan, *Phys. Rev. B* **2017**, *96*, 161201; b) T. Feng, X. Ruan, *Phys. Rev. B* **2018**, *97*, 045202; c) X. Gu, Z. Fan, H. Bao, C. Y. Zhao, *Phys. Rev. B* **2019**, *100*, 064306.

[44] S. Kim, K. Kang, S. Y. Kim, *J. Mech. Phys. Solids* **2020**, *145*, 104166.

[45] W. Zhao, K. Jin, L. Fu, Z. Shi, B. Xu, *Nano Lett.* **2022**, *22*, 4750.

[46] W. Liu, S. Bai, *J. Materiomics* **2019**, *5*, 321.

[47] Y. Xing, R. Liu, J. Liao, C. Wang, Q. Zhang, Q. Song, X. Xia, T. Zhu, S. Bai, L. Chen, *Joule* **2020**, *4*, 2475.

[48] a) G. Kresse, J. Furthmüller, *Comput. Mater. Sci.* **1996**, *6*, 15; b) G. Kresse, J. Furthmüller, *Phys. Rev. B* **1996**, *54*, 11169.

[49] J. P. Perdew, K. Burke, M. Ernzerhof, *Phys. Rev. Lett.* **1996**, *77*, 3865.